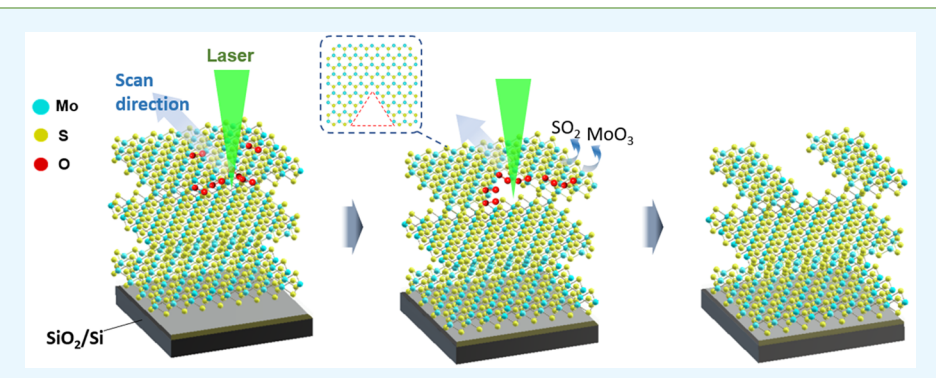


Site-Selective Atomic Layer Precision Thinning of MoS2 via Laser-**Assisted Anisotropic Chemical Etching**

Yoonsoo Rho, Jiayun Pei, Letian Wang, Zhengliang Su, Matthew Eliceiri, and Costas P. Grigoropoulos*, To

Supporting Information



ABSTRACT: Various exotic optoelectronic properties of two-dimensional (2D) transition metal dichalcogenides (TMDCs) strongly depend on their number of layers, and typically manifest in ultrathin few-layer or monolayer formats. Thus, precise manipulation of thickness and shape is essential to fully access their potential in optoelectronic applications. Here, we demonstrate site-selective atomic layer precision thinning of exfoliated MoS₂ flake by laser. The oxidation mediated anisotropic chemical etching initiated from edge defects and progressed by controlled scanning of the laser beam. Thereby, the topmost layer can be preferentially removed in designed patterns without damaging the bottom flake. In addition, we could monitor the deceleration of the thinning by in situ reflectance measurement. The apparent slow down of the thinning rate is attributed to the sharp reduction in the temperature of the flake due to thickness dependent optical properties. Fabrication of monolayer stripes by laser thinning suggests potential applications in nonlinear optical gratings. The proposed thinning method would offer a unique and rather straightforward way to obtain arbitrary shape and thickness of a TMDCs flake for various optoelectronic applications.

KEYWORDS: TMDCs, MoS2, laser thinning, single-layer precision thinning, anisotropic chemical etching, nonlinear optical grating

INTRODUCTION

Two-dimensional (2D) transition metal dichalcogenides (TMDCs) are atomically thin semiconductors showing exceptional optoelectronic and electronic properties, including relatively large direct band gap (1.1-1.9 eV), chirality in photoluminescence, and strong nonlinear optical response, which originate from their strongly confined electron profiles in 2D structures. 1-9 Thus, their unique and highly promising characteristics primarily depend on their thickness and typically appear in ultrathin few layers or monolayers. In addition, ultrathin layers mechanically exfoliated from bulk crystals possess high crystallinity. However, the mechanical cleavage of bulk crystals relies on a spatially random van der Waals force between the TMDC material and the transfer substrate. 10 This fact results in uncontrollable thickness and random shape with low yield, which consumes considerable time and, thus, limits various applications with designed patterns.

To this end, a variety of methods to control the thickness of the exfoliated TMDC flake have been employed, including plasma treatment, 11-13 chemical 14-18 or thermal 19 etching assisted by heating, and laser-induced local treatment.^{20–22} Among these methods, the laser has been regarded as the most feasible means to induce selective patterning of thinned exfoliated TMDCs. 20-22 Lasers can provide spatially and temporally confined temperature profiles site-selectively to promote either a thermal process or a chemical reaction at micrometer scales without expensive CMOS fabrication methods. Castellanos-Gomez et al. first introduced laser methods for the thinning of MoS₂ and attributed the thinning mechanism to the lateral thermal sublimation by high laser fluence $(30-80 \text{ mW}/\mu\text{m}^2)$.²⁰ This purely thermal process

Received: August 10, 2019 Accepted: September 25, 2019 Published: September 25, 2019



Laser Thermal Lab, Department of Mechanical Engineering, University of California, Berkeley, California 94720, United States [‡]Department of Mechanical Engineering, Tsinghua University, Beijing 100084, People's Republic of China

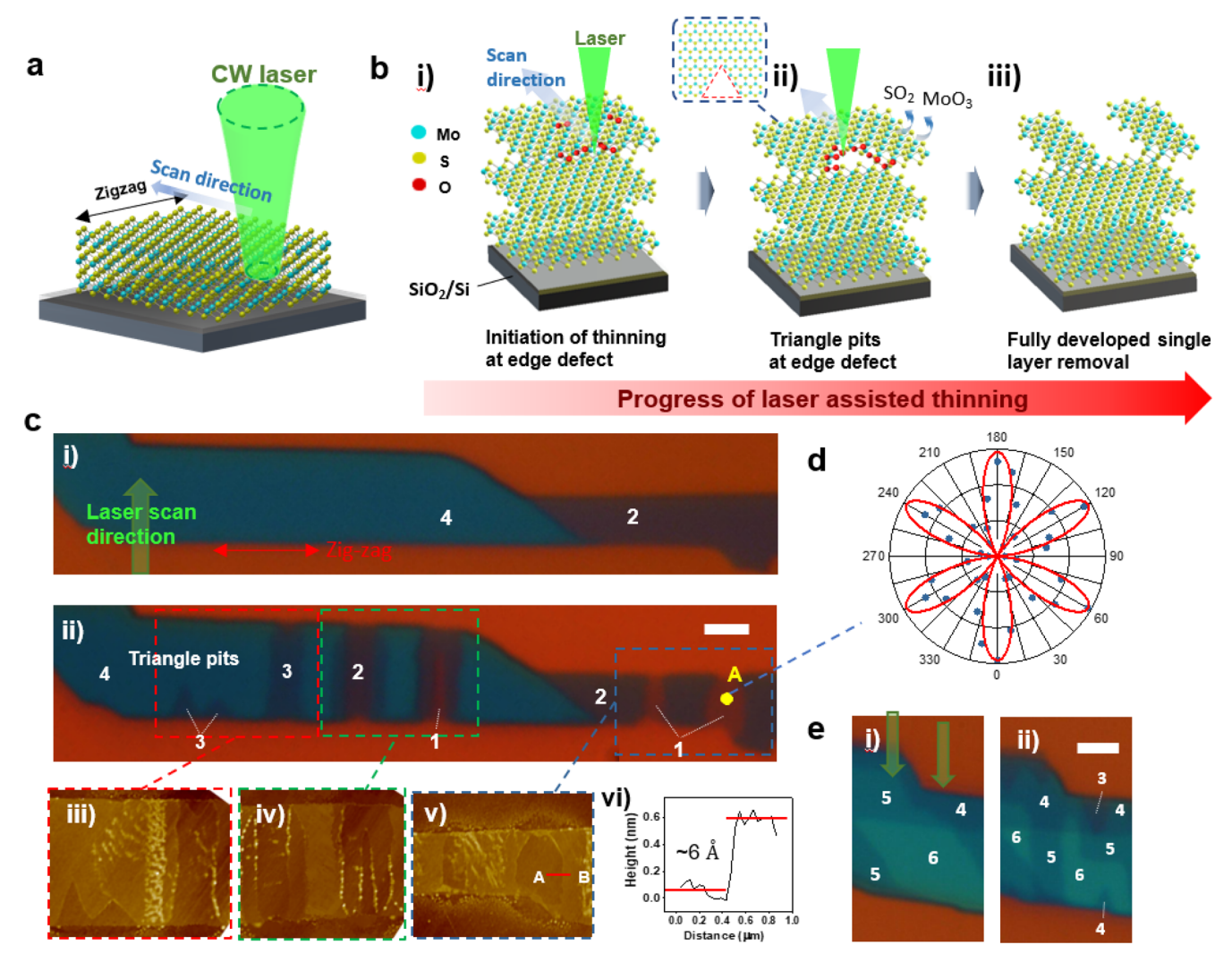


Figure 1. Overall concepts and results of the site-selective atomic precision thinning of MoS_2 by laser-induced anisotropic etching. (a) Schematics of laser irradiation from the edge of the MoS_2 flake. (b) Schematics of the thinning process initiated by edge defect aided by oxygen mediated chemical etching process. (i) Initiation of thinning at edge defect, (ii) triangle pits appearing at the edge defects while producing volatile SO_2 and MoO_3 substances, and (iii) fully developed single-layer removal without damage to bottom flake. (c) Experimental results of the thinning process with optical microscope images of pristine (i) and post-thinning (ii) MoS_2 . The AFM images taken from the dashed boxes in panel c(ii) show the thinned tri- (iii) and bi- and monolayers (iv) from the tetralayer region, and the thinned monolayer from the bilayer region (v) by 2.1, 2.8, 3.1, 3.5, and 4.7 mW/ μ m², respectively. The lateral height profile measured along the A–B line in panel c(v) show monolayer thickness \sim 6 Å (vi). (d) Angularly resolved optical SHG intensity plot measured from A point in yellow color in panel c(ii). The blue dots indicate measured SHG intensity, while the red line shows curve fitting to the theoretical value. (e) Optical images of pristine (i) and thinned (ii) MoS_2 flake by 2.1 mW/ μ m² laser fluence at 2 μ m/s travel speed. The scale bars indicate 1 μ m.

lacks thickness control at single-layer precision, e.g., produced monolayer directly from few-layer crystals. Alternatively, lasers can selectively promote chemical reactions on the topmost layer by introducing chemical substances. In addition, the chemical reaction typically requires lower temperatures than thermal sublimation, which would enable single-layer removal without sacrificing properties of the bottom layer. For example, Nagareddy et al. demonstrated layer-by-layer thinning of MoTe₂ by low laser fluence $(0.3-4 \text{ mW}/\mu\text{m}^2)$ aided by adsorbed water vapor on the surface of the flake.²¹ This result was partly ascribed to the vulnerable thermal and chemical stability of MoTe2 due to the low electronegativity difference between Mo and Te, $(\Delta \chi \sim 0.3)^{23-26}$ Other inert TMDCs such as MoS₂ and WSe₂ with stronger interatomic bonding $(\Delta \chi \sim 0.7)$ would require an additional strategy for a reliable single-layer removal process.

Notably, by furnace annealing in an oxygen environment, disconnected etched pits can be generated in MoS_2 and WSe_2 by oxygen mediated anisotropic chemical etching at relatively low temperature (\sim 550 K). The etched pits appear from either randomly distributed intrinsic chalcogen vacancies or edge defects. On the basis of density functional theory (DFT) calculations, oxygen molecules can be dissociated and physisorbed preferentially at the S-vacancy and edges of MoS_2 at the low chemical energy barrier ($E_a \sim 0.8$ and 0.3 eV, respectively, compared to \sim 1.6 eV for the pristine surface), which can spontaneously occur even at room temperature and be further promoted by heating. Thus, utilizing chemical etching initiated by defects in conjunction with the laser scanning would allow a new pathway to the controllable and single-layer precision thinning of MoS_2 .

Herein, we demonstrated the atomic layer precision thinning of MoS₂ by defect-initiated laser-induced chemical etching in

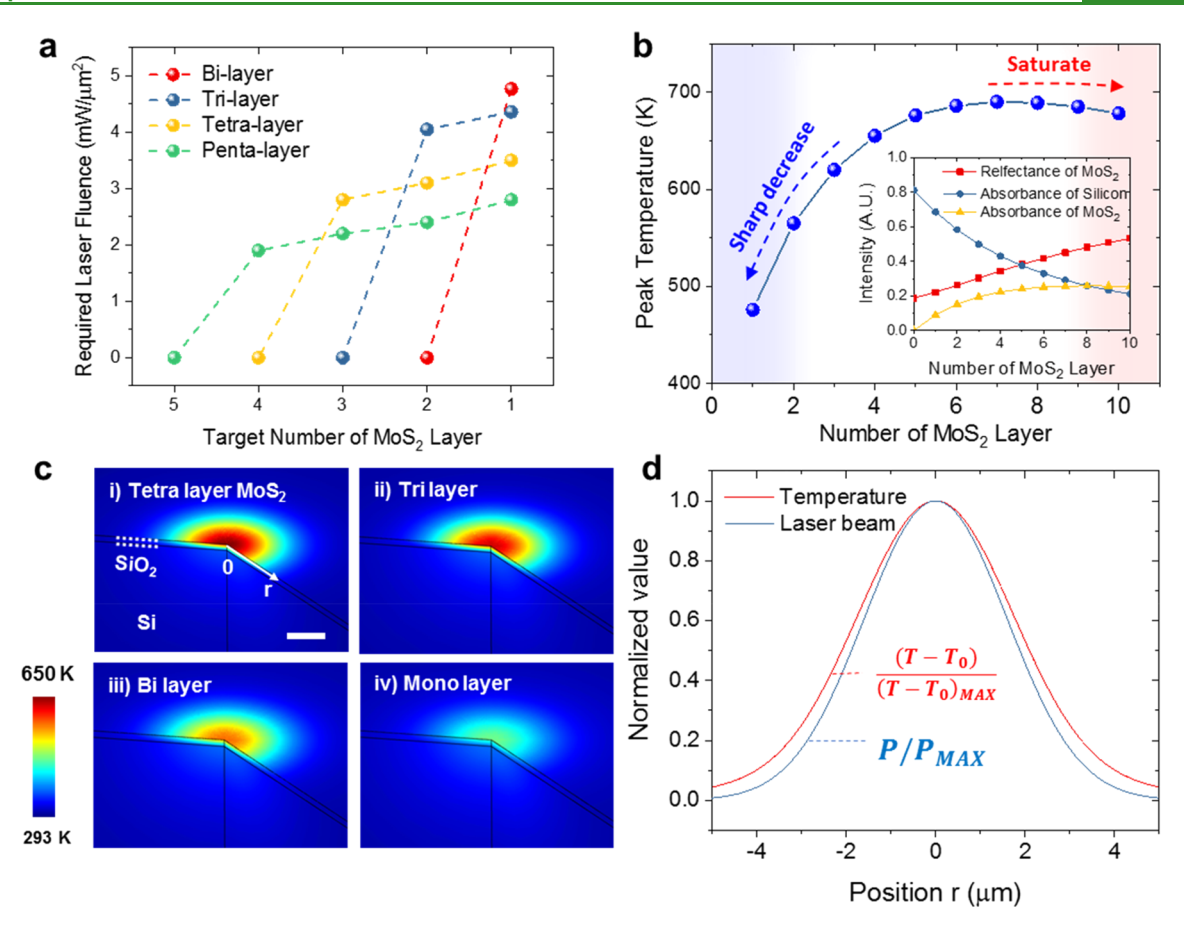


Figure 2. Laser conditions and heat transfer modeling of the laser-induced thinning process showing the self-limited thinning process and strong spatial confinement. (a) Required laser power of the thinning process versus the target number of layers of MoS₂ flakes for various starting flakes with bi-, tri-, tetra-, and pentalayers. (b) Simulated peak temperature of MoS₂ versus number of layers of MoS₂ flakes in the case of irradiation at 3.1 mW/ μ m² of the laser beam. The inset shows the calculated reflectance and absorbance of MoS₂ and absorbance of Si based on the thin film optics at 532 nm wavelength in the case of MoS₂/SiO₂(300 nm thick)/Si multilayer system. (c) Simulated temperature field of tetra-, tri-, bi-, and monolayer MoS₂ based on the same simulation method and laser condition used in panel b. The scale bar indicates 2 μ m. (d) Normalized temperature and laser power profiles along the r direction indicated in panel c(i).

ambient condition. In the case of laser irradiation from the edge defects, a most prevalent and easily accessible form of defect, the anisotropically etched pits along specific lattice orientation can be generated from the edges at relatively low laser irradiance (2-4 mW/ μ m²). The scanning of the laser beam across the flake allowed the realization of the continuously developed single-layer removal. In addition, we investigated the deceleration of the laser-induced thinning process by the heat transfer simulation and in situ reflectance measurement. The transient change of the optical properties of MoS₂ during thinning sharply reduce the temperature increase, mitigating the thinning process. Finally, we fabricated periodic thinned stripe patterns in the MoS₂ flake, showing potential for nonlinear optical grating applications. Thus, our work may open a new venue to expand applicability of the TMDC materials by providing a robust method to control the thickness and shape in a site-selective manner.

■ RESULTS AND DISCUSSION

Few-layer MoS_2 flakes were isolated on Si/SiO_2 (300 nm thick) wafers by the mechanical exfoliation method. Prior to the laser thinning process, the thickness of the flake was determined by atomic force microscopy (AFM) and Raman spectroscopy. The continuous wave (CW) laser beam at 532 nm wavelength was focused at the size of 6.4 μ m (1/e²)

diameter through an objective lens (NA $\sim 0.28)$ and scanned across the MoS_2 flake at 2 $\mu m/s$ of travel speed in ambient condition. As shown in Figure 1a, the laser scanning started outside of the flake to initiate etched pits from edge defects. The CW laser beam irradiation can effectively induce a locally confined temperature profile in a microscale area. The low thermal diffusivity of SiO $_2$ layers ($\sim \! 100 \text{ W/mK})$ and low thermal boundary conductance between MoS $_2$ flakes and SiO $_2$ ($\sim \! 20 \text{ MW/m}^2 \text{K}^{30}$) contribute to the local temperature confinement.

After scanning the CW laser beam across the edge of the tetralayer flake, single- or few-layer removal can be clearly observed as shown in Figure 1c. As laser power increased and exceeded the threshold to initiate thinning from the edge (\sim 2.1 mW/ μ m²), triangular pits on the topmost layer could emanate from the edge of MoS₂ flake (Figure 1c(iii)). At higher laser power, 2.8 mW/ μ m², the etched pit propagated along the laser irradiation trajectory yielding a fully developed thinned trilayer region. As we further increased laser power, even thinned bi- and monolayers at 3.1 and 3.5 mW/ μ m², respectively, can be clearly observed, indicating atomic layer precision thinning in a locally selective area (Figure 1c(iv)). Similar to the tetralayer case, monolayer thinned regions from the bilayer can be demonstrated, while higher laser power 4.7 mW/ μ m² was required due to different absorbance depending

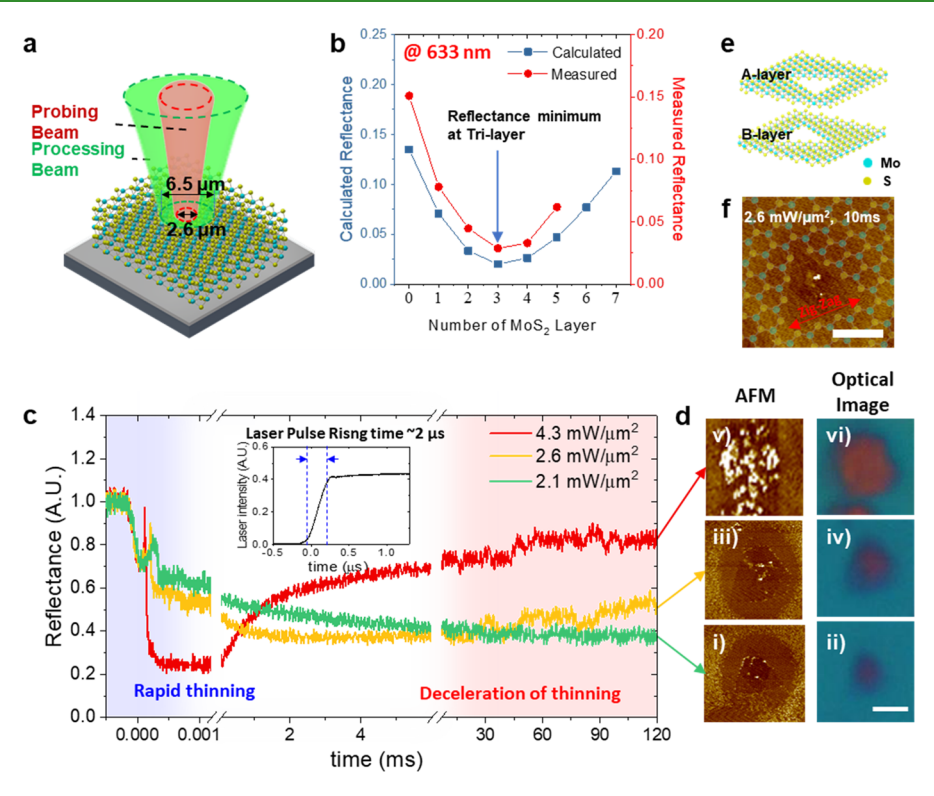


Figure 3. Time-resolved reflectance measurement supporting the self-limited thinning process. (a) Schematics of time-resolved reflectance measurement consisting of coaxially aligned 532 nm of the processing beam $(2\omega \sim 2.6 \ \mu\text{m})$ and 633 nm of the probing beam $(2\omega \sim 6.4 \ \mu\text{m})$. (b) Calculated and measured reflectance of MoS₂ flake depending on the number of layers. The reflectance minimum occurs at the trilayer thickness. (c) Measured time-resolved reflectance data during laser thinning depending on the laser power of 2.1, 2.6, and 4.3 mW/ μ m². The starting flake was the penta(5)layer. The inset graph shows the temporal profile of the processing laser pulse, showing 2 μ s of rising time. (d) AFM and optical images of thinned MoS₂ by laser power, 2.1 (i, ii), 2.6 (iii, iv), and 4.3 mW/ μ m² (v, vi). (e) Schematics of thinned 2H phase of MoS₂ showing opposite direction of triangle pits. (f) AFM image of MoS₂ after thinning at 2.6 mW/ μ m² for 10 ms shows the opposite direction of the thinned area in adjacent layer. The semitransparent MoS₂ lattice structure shows the zigzag edges of triangle pits. The scale bars in this figure are 1 μ m.

on the number of layers of the starting flake (Figure 1c(v)). The height profile from the thinned monolayer region to the pristine bilayer (along the AB line in Figure 1c(iii)) depicts the single-layer thickness of MoS $_2\sim 6$ Å (Figure 1c(vi)), providing strong evidence of the atomic layer removal by laser processing.

The single-layer precision thinning performed in Figure 1 can be ascribed to oxidation mediated etching of MoS₂, initiated at the edge defect as schematically illustrated in Figure 1b. Previous reports about furnace annealing of MoS₂ in an oxygen environment suggested that randomly distributed intrinsic defects and edge defects can serve as initiation sites for oxidation-induced anisotropic etching. 14-18 This can be understood with the low energy barrier for the reaction of oxygen molecules at S-vacancy sites and edges (0.8 and 0.31 eV, respectively, for the Mo zigzag edge), whereas the pristine MoS₂ surface exhibits higher energy barrier (1.6 eV).²⁷ Thus, the oxygen reaction initiated by the defects produces volatile substances including SO₂ and MoO₃. As the edge defects are identified and located, the etching from the edge is easily controllable and repeatable (Figure 1e), while the etched pits from the middle of the flake were randomly generated from intrinsic S-vacancy defects (Supporting Information Figure S1). Thus, initial pits could be generated from the edge by laser irradiance at 2.1 mW/ μ m², but the thinning stopped at the middle of the flake as the slower etching propagation could not keep pace with the laser scanning. On the other hand, laser irradiance at 2.8 mW/ μ m² can develop the continuous thinned

region due to the faster chemical reaction at higher induced temperature as shown by furnace annealing. 14,15 In addition, despite a much shorter laser dwell time (~3 s) than that of furnace annealing (~2 h), the etched pits obtained by laser have comparable size to the pits obtained by furnace annealing. This can be understood by the enhanced oxygen molecule supply by three-dimensional diffusion process toward the tightly focused laser spot, whereas the one-dimensional chemical supply would limit the reaction rate in furnace annealing.³¹ Also, it is noted that the triangle shape implies the 3-fold lattice symmetricity of MoS2, which belongs to the P6m2 space group. Thus, the lattice orientation of the triangular pits should be along either the S or Mo zigzag edge (1120) of the MoS₂ flake, whereas the armchair edge $\langle 10\overline{1}0 \rangle$ would result in a hexagonal shape. However, the exact termination of edge (e.g., S or Mo zigzag) cannot be determined and requires further investigation.

To probe the crystalline orientation of the triangle pits and evaluate the quality of the thinned monolayer, we acquired a polar plot of optical second harmonic generation (SHG) intensity as a function of the crystal's azimuthal angle from the thinned MoS₂ monolayer (at the spot A in Figure 1c(ii)). SHG measurement was employed since it can provide non-destructive means to determine the crystalline orientation and quality of the MoS₂ flake. As the whole 2H phase flake shown in Figure 1 was exfoliated from the single bulk crystal, the thinned monolayer and triangle pits appearing in the tetralayer should manifest identical lattice orientation. We

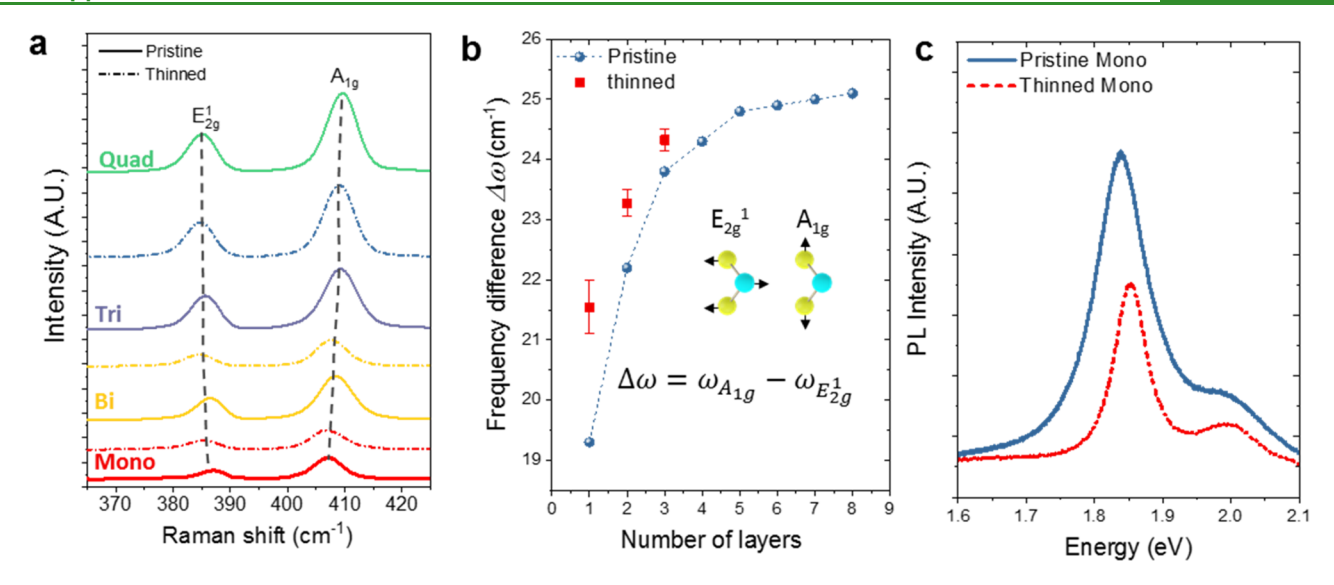


Figure 4. (a) Raman spectra of mono-, bi-, tri-, and tetralayers of pristine (solid line) and thinned (dashed line) MoS₂ flakes. (b) Frequency difference between A_{1o} and E_{2o}^1 of pristine and thinned MoS₂ depending on the number of layers. (c) PL spectra of pristine and thinned monolayers.

performed angularly resolved SHG measurement as shown in Figure 1d (the details are in Methods). The 6-fold symmetricity was clearly preserved on monolayer MoS₂, which strongly supports that the crystallinity of the thinned monolayer was intact without significant lattice distortion or strain. In addition, the SHG plot from the thinned monolayer has a maximum value at the edge direction and it implies that the triangle pits have zigzag edges, 4,5 since they originated from single MoS₂ crystals.

Figure 2a depicts the required laser power to produce MoS₂ layers of target thickness from initial flakes of various thickness by edge-initiated laser thinning. The thicker the initial flake, the lower the required laser power to initiate thinning. Correspondingly, higher threshold laser power density is required to sustain the progress of the thinning process. This higher sensitivity of the thicker MoS₂ to the laser power (e.g., having the lower threshold power) can be attributed primarily to the thickness dependent optical properties of MoS₂. Furthermore, the thermal conductivity of MoS2 increases with the layer thickness and therefore the transverse heat loss should also increase. As a result, we found that the laser thinning is self-regulating, exhibiting deceleration and eventual cessation of etching. To estimate the laser-induced temperature depending on the thickness of MoS2, we calculated the absorbance of MoS₂ and Si by using thin film optics³² in the case of the MoS₂/SiO₂(300 nm)/Si multilayer as shown in the inset of Figure 2b (details are in Methods). Although the absorbance of MoS₂ is lower than that of silicon, it dominates the temperature transient and the peak temperature due to the much lower thermal mass $(\sim \rho C_p V)$ of the few-layers MoS₂ flake compared to the heat affected volume of silicon (\sim 1 μ m of optical absorption depth at 532 nm) as shown in the heat transfer modeling by using finite element method (FEM) (Figure 2c). Thus, as the thickness of MoS₂ reduced, the peak temperature of the MoS₂ flake sharply decreased (Figure 2b,c). Figure 2c displays steady state temperature distributions under identical laser irradiance of 3.1 mW/ μ m². The observed 230 K of temperature difference between tetra- and monolayers, is sufficient to arrest the etching process. This self-limited etching process can allow precise control of the number of layers,

which is not possible by other blank heating methods (e.g., furnace annealing). In addition, the temperature field induced by the laser can be tightly confined. In Figure 2d, the normalized temperature $(T - T_0)/(T - T_0)_{MAX}$ and laser power P/P_{MAX} are plotted along the r direction indicated in Figure 2c(i) in the case of the tetralayer. The predicted full width at half-maximum (fwhm) of the temperature field is 4.2 μ m, which is slightly larger than 3.7 μ m of fwhm of the laser beam spot $(\sim \sqrt{\ln 2/2} (2w))$, where 2w is $1/e^2$ width, $6.4 \mu m)$. Apart from the effect of the temperature drops during the thinning process, the self-limited behavior can be partly ascribed to the strong coupling energy between the MoS₂ and SiO_2 interface compared to that of MoS_2 interlayers as suggested by Wang et al.¹⁸ This mechanism can further increase the threshold laser power by stabilizing the substrate— MoS₂ system when it thinned down.

To investigate the details of transient characteristics of laserinduced thinning process, we performed in situ reflectance measurement as shown in Figure 3. We utilized a 633 nm He-Ne CW laser as a probing beam with a 2.6 μ m (1/e²) spot size, which is sufficiently smaller than the size of processing laser beam spot (6.4 μ m) at 532 nm, allowing precise measurement of transient thickness change of MoS2 flakes. In addition, the thinning process was performed in the middle of the MoS₂ flakes without scanning the laser beam (Figure 3a). The Gaussian-like temperature profiles induced by the laser beam initiated defect sites at the center of the flakes and induced laterally expanding triangular pits. The temporal shape of the laser pulse was precisely controlled by acoustic optical modulator (AOM), providing fast rising and decaying time (\sim 2 μ s as shown in the inset of Figure 3c). The details of the optical setup are provided in Figure S3. Prior to the measurement, the reflectance of the MoS₂/SiO₂(300 nm)/Si multilayer at 633 nm was calculated by using thin film optics³² (details are in Methods), and it is well-matched with the measured reflectance value as shown in Figure 3b. The reflectance value touched its minimum at a trilayer of MoS₂, which can be utilized as a reference point to track the thickness of MoS₂ during the thinning process. Figure 3c depicts measured in situ reflectance change during the thinning

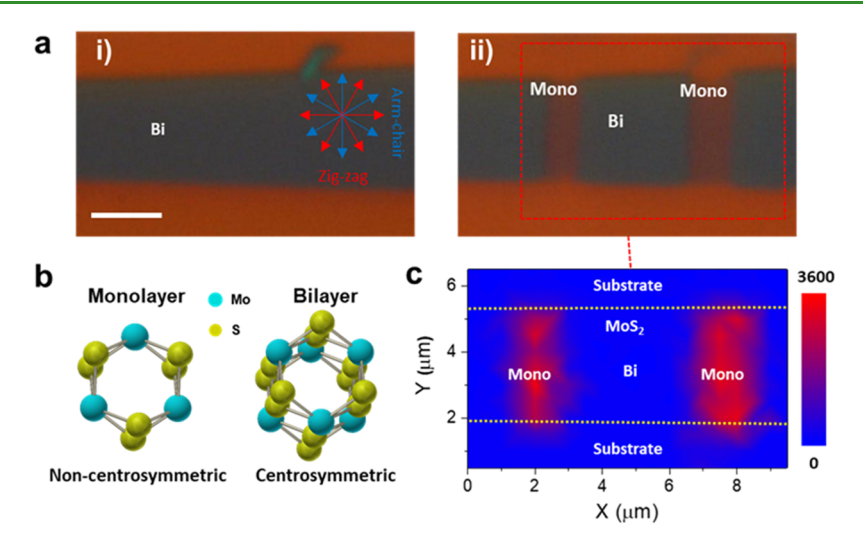


Figure 5. Example of nonlinear optical grating based on site-selective thinned monolayer from bilayer MoS₂ flake. (a) Optical microscopy images of pristine (i) and thinned (ii) MoS₂ flake. The scale bar indicates 2 μ m. (b) Schematics of mono- and bilayers of 2H phase MoS₂. (c) SHG mapping images from red dashed box in panel a(ii) showing strong SHG contrast.

process starting from pentalayers of MoS2 flakes by using varied laser power. At 2.1 mW/ μ m² of laser irradiance, the reflectance decreased slowly and reached its lowest point at the end of the process (~100 ms), which indicates that the thinning process reached the trilayer stage. The resulting AFM and optical images (Figure 3d(i,ii)) showed that the triangle pits were generated from the center region of the laser beam spot where initial defects can be preferentially generated due to the highest induced temperature. It is noted that the triangle pits at a 180° rotated direction appeared in adjacent layers, indicating that the etching process occurred along either S or Mo zigzag edges due to the opposite stacking order of the 2H phase of MoS_2 .⁶ As laser irradiance increased to 2.6 mW/ μ m², the reflectance minimum was obtained at 3 ms and increased slowly within a time frame of 100 ms. The acquired AFM and optical images (Figure 3d(v,vi)) showed that the thinning process produced bi- and monolayers with a well-defined triangle shape. This indicates that the thinning process produced a trilayer at ~3 ms and the temperature reduction due to a thinner MoS2 layer decelerated the thinning process, which supports the self-limiting behavior predicted by our heat transfer modeling. Also, the results imply that the etching rate largely depends on the laser power. As the laser irradiance increased to higher value (4.3 mW/ μ m²), the reflectance abruptly decreased at the very initial stage (<1 μ s) and bounced back to higher values gradually. The resulting flake presented the isotropic area removal with a rough surface (Figure 3d(iii,iv)). The fast reflectance drops and contrasting morphology observed at high laser fluence can be attributed to the thermal sublimation which is fundamentally different from the chemical etching reaction. At this processing region, controlled and well-defined thinned MoS2 flakes are difficult to obtain due to a violent material ablation process.

In Figure 4a, Raman spectra of pristine and thinned MoS_2 layers at various thicknesses are depicted. The out-of-plane (A_{1g}) phonon vibration modes are slightly blue-shifted, while the peak positions of A_{1g} of thinned mono-, bi-, and trilayers were upshifted by 2, 1.6, and 0.7 cm⁻¹, respectively, compared to that of the pristine state of MoS_2 . This change of A_{1g} peak position can be ascribed to the electron withdrawal by oxygen doping due to processing under ambient conditions.³³ On the

other hand, in-plane $(E_{2\sigma}^1)$ mode did not show much difference between thinned and pristine MoS₂ flakes. In addition, the peak position differences $(\omega_{\rm A_{ig}}-\omega_{\rm E2g}^{-1})$ of pristine and thinned flakes are plotted in Figure 4b as it can be a useful indicator to determine the number of layers of MoS₂. 34 The values of the thinned monolayer located between pristine mono- and bilayer flakes. Also, the values of thinned tri- and bilayer showed a trend similar to that of pristine flakes as well. Thus, it is deduced that thinning was achieved, while oxygen doping effects cannot be excluded. In addition, strong photoluminescence (PL) can be measured from a thinned monolayer (Figure 4c). Compared to the pristine monolayer, the peak position was clearly blue-shifted (15 meV), which can be attributed to p-type doping effect due to electron withdrawal by oxygen, leading to transition from negative trion X⁻ to neutral exciton X⁰ dominated states.³⁵ The slight decrease of peak intensity is due to the increase of defect sites inducing a nonradiative recombination.³⁶

The thinned TMDCs by laser can be used for nonlinear optical grating applications. A periodic modulation of second harmonic susceptibility, $\chi^{(2)}$, can induce multiorder nonlinear diffraction, analogous to the Bragg diffraction from the dielectric materials with periodic refractive index, generally termed as photonic crystals.^{37–39} In the case of TMDCs, due to the broken inversion symmetry of the 2H phase, an odd number of layers can induce strong SHG signals, whereas an even number of layers with opposite stacking orders of the adjacent layers establishes the centrosymmetricity and forbids the SHG (Figure 5b). Thus, single-layer thinning of TMDCs in designed patterns will provide periodically aligned flakes with odd and even numbers of layers, which can be utilized for SHG grating platforms. As shown in Figure 5a, starting from the pristine bilayer, we patterned a \sim 1.5 μ m width of a thinned monolayer with a 4.2 μm gap. From this patterned flake, the SHG mapping image can be obtained without an analyzer (e.g., detect the total SHG intensity; Figure 5c). Strong SHG intensity can be obtained only from thinned monolayers, while pristine bilayers produced negligible signal intensity that is similar to the background intensity from the substrate.⁴ We expect that starting from scalable even-layer MoS2 flakes produced by the CVD method, the controlled dimension of periodic thinned odd layers can be fabricated at micrometer scale as a feasible approach to offer high quality and scalable nonlinear optical grating systems.

CONCLUSIONS

In summary, we demonstrated the site-selective atomic layer precision thinning of MoS₂ by laser-induced anisotropic chemical etching. The oxygen mediated chemical etching initiated from edge defects enabled a controllable and repeatable thinning process. The self-limited thinning of MoS₂ was investigated by heat transfer analysis that showed a sharp decrease of the temperature upon thinning. This was supported by transient in situ reflectance measurement. The potential use of the thinned MoS2 in a nonlinear optical grating was demonstrated by fabrication of a monolayer stripe from a bilayer MoS₂ flake. Our investigation of the laser thinning offers insight into the laser-assisted processing of TMDCs, which can proceed via chemical reactions or a thermal sublimation. In addition, we believe that the proposed selflimited and defect-initiated chemical etching by laser may offer a unique route to atomic layer precision thinning of common TMDCs.

METHODS

Laser Processing. Diode-pumped solid state (DPSS) CW laser at 532 nm wavelength (Sprout-C, Sprout) was focused through a $20 \times (NA \sim 0.28)$ objective lens. A dichroic mirror in the middle of the beam path allows in situ monitoring of the MoS_2 flake during thinning. A motorized XY linear stage at 100 nm resolution (Aerotech) was utilized for the laser scanning.

Raman Measurement. A Raman system (inVia, Renishaw) equipped with 532 nm wavelength was utilized with 1800 g/mm resolution of grating. The laser power was kept at 0.5 mW during the Raman measurement.

SHG Measurement. A Ti:sapphire femtosecond laser (Tsunami, Spectra physics, $\lambda \sim 800$ nm, $f \sim 80$ MHz) was utilized for the SHG characterization. Low laser power below 100 µW was utilized to avoid any potential damage on the flake. The polarization of the input laser beam was manipulated by a half-wave plate, while the polarization of the detected SHG signal was selected via polarizer. A photomultiplier tube collected the SHG signal intensity at 400 nm and synchronized with the XY stage when mapping was performed. For angularly resolved SHG measurement, the polarization of the pump laser beam was aligned parallel to the analyzer of the photon detector. The intensity of SHG from the MoS_2 monolayer can be fitted to $I = I_0$ $\cos^2(3\theta)$, where θ denotes the angle between the direction of the zigzag and the polarization of the pump laser beam and I_0 is the maximum SHG intensity. In this measurement configuration, the angularly resolved SHG should have a maximum value at the direction of the zigzag edge ($\theta \sim n\pi/3$) with 6-fold symmetricity.⁴

Calculation of Optical Properties. We use notations 0, 1, 2, and 3 for air (vacuum), MoS₂, SiO₂, and Si, respectively. The complex refractive indices of layers are indicated as follow. $n_0 = 1$, $n_1 = 4.8-1.1i$, $n_2 = 1.4$, and $n_3 = 4.2-0.4i$.

By using Fresnel's equation, the reflectivity and transmissivity at each boundary can be obtained. ⁴¹ (1, 2, and 3 indicate interfaces between Air and MoS₂, MoS₂, and SiO₂, and SiO₂ and Si, respectively)

$$r_1 = \frac{n_0 - n_1}{n_0 + n_1}$$
 $r_2 = \frac{n_1 - n_2}{n_1 + n_2}$ $r_3 = \frac{n_2 - n_3}{n_2 + n_3}$

$$t_1 = \frac{2n_0}{n_0 + n_1}$$
 $t_2 = \frac{2n_1}{n_1 + n_2}$ $t_3 = \frac{2n_2}{n_2 + n_3}$

Considering multireflection and transmission at the interfaces, by using transfer matrix calculation, the total reflectivity, r_{MoS_2} , and absorptivity of silicon, $a_{\text{S}i}$, can be obtained as follows.

$$r_{\text{MoS}_2} = \frac{r_1 + r_2 Z_1^{-2} + r_1 r_2 r_3 Z_2^{-2} + r_3 Z_1^{-2} Z_2^{-2}}{1 + r_1 r_2 Z_1^{-2} + r_2 r_2 Z_2^{-2} + r_1 r_3 Z_1^{-2} Z_2^{-2}}$$

$$a_{\text{Si}} = \frac{t_1 t_2 t_3 Z_1^{-1} Z_2^{-1}}{1 + r_1 r_2 Z_1^{-2} + r_2 r_3 Z_2^{-2} + r_1 r_3 Z_1^{-2} Z_2^{-2}}$$

where $Z_1=\mathrm{e}^{2\pi n_1 d_1/\lambda}$, $Z_2=\mathrm{e}^{2\pi n_2 d_2/\lambda}$, d_1 and d_2 are thicknesses of MoS₂ and SiO₂ layers, respectively, and λ is the wavelength of incoming light.

Finally, the total reflectance, $R_{\rm MoS,y}$ and absorbance, $A_{\rm Si}$, can be calculated as follows.

$$R_{\text{MoS}_2} = |r_{\text{MoS}_2}^* r_{\text{MoS}_2}|$$

$$A_{\rm Si} = Re \left(\frac{n_3}{n_0}\right) |a_{\rm Si}^* a_{\rm Si}|$$

If we consider the energy conservation and assume no power dissipation in the SiO_2 layer, the absorbance power ratio of MoS_2 , A_{MoS} , can be expressed as follows.

$$A_{\text{MoS}_2} = 1 - R_{\text{MoS}_2} - A_{\text{Si}}$$

By taking 532 and 633 nm as the wavelengths, 0.6 Å as the single-layer thickness of MoS_2 , and 300 nm as the SiO_2 layer, the absorbance and reflectance of MoS_2 and Si can be obtained.

Heat Transfer Simulation. The monolayer MoS_2 thickness, t_{MoS_2} was taken as ~ 6 Å and the thermal boundary conductance, g, between MoS_2 and SiO_2 was taken as ~ 20 MW/($m^2 \cdot K$). Thermal conductivity, k, density, ρ , and heat capacitance, C_p of MoS_2 , SiO_2 , and Si are summarized in Table S1. The governing equation, boundary condition, and initial condition for thermal simulations are as follows.

governing equation:

$$\rho C_p \frac{\partial T}{\partial t} = k \nabla^2 T + Q$$

initial condition:

$$T(t=0) = T_0$$

boundary condition:

(a)
$$T_{\text{bottom surface}} = T_0$$

(b)
$$k \frac{\partial T}{\partial r} \Big|_{r=R} = \varepsilon \sigma (T^4 - T_0^4)$$

(c)
$$k \frac{\partial T}{\partial z} \Big|_{\text{top surface}} = \varepsilon \sigma_{s} (T^{4} - T_{0}^{4})$$

where ε and σ_s are emissivity (assumed as 1) and the Stefan–Boltzmann constant (5.67 \times 10⁻⁸ W/(m²·K⁴)).

In addition, the laser flux absorbed by MoS_2 in the Gaussian laser beam profile was expressed as

$$Q = A_{\text{MoS}_2} I_{\text{peak}} e^{-(2r^2/w^2)}$$

where $A_{\rm MoS_2}$, $I_{\rm peak}$, and w indicate absorbance of MoS₂, laser peak intensity, and laser beam size, respectively. Also, Beer–Lambert Law was considered in this simulation. The absorption coefficient of silicon, $a_{\rm Si}$ at 532 nm is \sim 7.85 \times 10³ cm⁻¹, and this can be reflected by following equation.

$$\frac{\partial I}{\partial z} = -a_{\rm Si}I$$

The cylindrical coordinate with steady state condition was applied to get the three-dimensional temperature profile.

In Situ Reflectance Measurement. The processing laser at 532 nm wavelength was temporally shaped within 2 μ s of rising and falling time by acoustic optical modulator (AOM). The probing laser at 633 nm was coaxially coupled with the probing laser by polarized beam splitter (PBS). The probing beam passes through the quarter wave plate (633 nm) two times, resulting in 90° rotation of the polarization of the reflected part compared to the input part. Thus, the 633 nm probing beam can path through the PBS to the photodetector. The color filter blocked the probing beam while allowing the probing beam to the detector. Another photodetector triggers an oscilloscope by the probing beam to capture the transient reflectance data during the laser thinning process. The schematics of the setup are described in Figure S3.

ASSOCIATED CONTENT

Supporting Information

The Supporting Information is available free of charge on the ACS Publications website at DOI: 10.1021/acsami.9b14306.

(Figure S1) Optical microscope images; (Figure S2) multiple reflection and transmission schematic; (Figure S3) optical setup schematics; (Figure S4) Raman spectra; (Table S1) thermal properties (PDF)

AUTHOR INFORMATION

Corresponding Author

*E-mail: cgrigoro@berkeley.edu.

ORCID ®

Costas P. Grigoropoulos: 0000-0002-8505-4037

Notes

The authors declare no competing financial interest.

ACKNOWLEDGMENTS

Financial support awarded to the University of California, Berkeley, by the U.S. National Science Foundation (Grant No. CMMI-1662475) is gratefully acknowledged.

REFERENCES

- (1) Liu, K.-K.; Zhang, W.; Lee, Y.-H.; Lin, Y.-C.; Chang, M.-T.; Su, C.-Y.; Chang, C.-S.; Li, H.; Shi, Y.; Zhang, H.; Lai, C.-S.; Li, L.-J. Growth of Large-Area and Highly Crystalline Mos2 Thin Layers on Insulating Substrates. Nano Lett. 2012, 12 (3), 1538-1544.
- (2) Yin, Z.; Li, H.; Li, H.; Jiang, L.; Shi, Y.; Sun, Y.; Lu, G.; Zhang, Q.; Chen, X.; Zhang, H. Single-Layer Mos2 Phototransistors. ACS Nano 2012, 6 (1), 74-80.
- (3) Splendiani, A.; Sun, L.; Zhang, Y.; Li, T.; Kim, J.; Chim, C.-Y.; Galli, G.; Wang, F. Emerging Photoluminescence in Monolayer Mos2. Nano Lett. 2010, 10 (4), 1271-1275.
- (4) Li, Y.; Rao, Y.; Mak, K. F.; You, Y.; Wang, S.; Dean, C. R.; Heinz, T. F. Probing Symmetry Properties of Few-Layer Mos2 and H-Bn by Optical Second-Harmonic Generation. Nano Lett. 2013, 13 (7), 3329-3333.
- (5) Malard, L.; Alencar, T.; Barboza, A. P. M.; Mak, K.; de Paula, A. Observation of Intense Second Harmonic Generation from Mos2 Atomic Crystals. Phys. Rev. B: Condens. Matter Mater. Phys. 2013, 87, 201401.
- (6) Wang, Q. H.; Kalantar-Zadeh, K.; Kis, A.; Coleman, J. N.; Strano, M. S. Electronics and Optoelectronics of Two-Dimensional Transition Metal Dichalcogenides. Nat. Nanotechnol. 2012, 7 (11),

- (7) Liu, W.; Liu, M.; OuYang, Y.; Hou, H.; Ma, G.; Lei, M.; Wei, Z. Tungsten Diselenide for Mode-Locked Erbium-Doped Fiber Lasers with Short Pulse Duration. Nanotechnology 2018, 29 (17), 174002.
- (8) Liu, W.; Zhu, Y.-N.; Liu, M.; Wen, B.; Fang, S.; Teng, H.; Lei, M.; Liu, L.-M.; Wei, Z. Optical Properties and Applications for Mos2-Sb2te3-Mos2 Heterostructure Materials. Photonics Res. 2018, 6 (3), 220 - 227.
- (9) Ou, G.; Fan, P.; Ke, X.; Xu, Y.; Huang, K.; Wei, H.; Yu, W.; Zhang, H.; Zhong, M.; Wu, H.; Li, Y. Defective Molybdenum Sulfide Quantum Dots as Highly Active Hydrogen Evolution Electrocatalysts. Nano Res. 2018, 11 (2), 751-761.
- (10) Guo, Y.; Liu, C.; Yin, Q.; Wei, C.; Lin, S.; Hoffman, T. B.; Zhao, Y.; Edgar, J. H.; Chen, Q.; Lau, S. P.; Dai, J.; Yao, H.; Wong, H. S. P.; Chai, Y. Distinctive in-Plane Cleavage Behaviors of Two-Dimensional Layered Materials. ACS Nano 2016, 10 (9), 8980-8988.
- (11) Kim, K. S.; Kim, K. H.; Nam, Y.; Jeon, J.; Yim, S.; Singh, E.; Lee, J. Y.; Lee, S. J.; Jung, Y. S.; Yeom, G. Y.; Kim, D. W. Atomic Layer Etching Mechanism of MoS2 for Nanodevices. ACS Appl. Mater. Interfaces 2017, 9 (13), 11967-11976.
- (12) Lin, T.; Kang, B.; Jeon, M.; Huffman, C.; Jeon, J.; Lee, S.; Han, W.; Lee, J.; Lee, S.; Yeom, G.; Kim, K. N. Controlled Layer-by-Layer Etching of MoS2. ACS Appl. Mater. Interfaces 2015, 7 (29), 15892-
- (13) Liu, Y.; Nan, H.; Wu, X.; Pan, W.; Wang, W.; Bai, J.; Zhao, W.; Sun, L.; Wang, X.; Ni, Z. Layer-by-Layer Thinning of Mos2 by Plasma. ACS Nano 2013, 7 (5), 4202-4209.
- (14) Yamamoto, M.; Einstein, T. L.; Fuhrer, M. S.; Cullen, W. G. Anisotropic Etching of Atomically Thin Mos2. J. Phys. Chem. C 2013, 117 (48), 25643-25649.
- (15) Zhou, H.; Yu, F.; Liu, Y.; Zou, X.; Cong, C.; Qiu, C.; Yu, T.; Yan, Z.; Shen, X.; Sun, L.; Yakobson, B. I.; Tour, J. M. Thickness-Dependent Patterning of Mos2 Sheets with Well-Oriented Triangular Pits by Heating in Air. Nano Res. 2013, 6 (10), 703-711.
- (16) Yamamoto, M.; Dutta, S.; Aikawa, S.; Nakaharai, S.; Wakabayashi, K.; Fuhrer, M. S.; Ueno, K.; Tsukagoshi, K. Self-Limiting Layer-by-Layer Oxidation of Atomically Thin Wse2. Nano Lett. 2015, 15 (3), 2067-2073.
- (17) Wu, J.; Li, H.; Yin, Z.; Li, H.; Liu, J.; Cao, X.; Zhang, Q.; Zhang, H. Layer Thinning and Etching of Mechanically Exfoliated Mos2 Nanosheets by Thermal Annealing in Air. Small 2013, 9 (19),
- (18) Wang, X.; Fan, W.; Fan, Z.; Dai, W.; Zhu, K.; Hong, S.; Sun, Y.; Wu, J.; Liu, K. Substrate Modified Thermal Stability of Mono-and Few-Layer Mos 2. Nanoscale 2018, 10 (7), 3540-3546.
- (19) Huang, Y.-K.; Cain, J. D.; Peng, L.; Hao, S.; Chasapis, T.; Kanatzidis, M. G.; Wolverton, C.; Grayson, M.; Dravid, V. P. Evaporative Thinning: A Facile Synthesis Method for High Quality Ultrathin Layers of 2d Crystals. ACS Nano 2014, 8 (10), 10851-
- (20) Castellanos-Gomez, A.; Barkelid, M.; Goossens, A. M.; Calado, V. E.; van der Zant, H. S. J.; Steele, G. A. Laser-Thinning of Mos2: On Demand Generation of a Single-Layer Semiconductor. Nano Lett. **2012**, 12 (6), 3187–3192.
- (21) Nagareddy, V. K.; Octon, T. J.; Townsend, N. J.; Russo, S.; Craciun, M. F.; Wright, C. D. Humidity-Controlled Ultralow Power Layer-by-Layer Thinning, Nanopatterning and Bandgap Engineering of Mote2. Adv. Funct. Mater. 2018, 28 (52), 1804434.
- (22) Lin, Z.; Ye, X.; Han, J.; Chen, Q.; Fan, P.; Zhang, H.; Xie, D.; Zhu, H.; Zhong, M. Precise Control of the Number of Layers of Graphene by Picosecond Laser Thinning. Sci. Rep. 2015, 5, 11662.
- (23) Zhu, H.; Wang, Q.; Cheng, L.; Addou, R.; Kim, J.; Kim, M. J.; Wallace, R. M. Defects and Surface Structural Stability of Mote2 under Vacuum Annealing. ACS Nano 2017, 11 (11), 11005-11014.
- (24) Li, Y.; Duerloo, K.-A. N.; Wauson, K.; Reed, E. J. Structural Semiconductor-to-Semimetal Phase Transition in Two-Dimensional Materials Induced by Electrostatic Gating. Nat. Commun. 2016, 7,
- (25) Diaz, H. C.; Chaghi, R.; Ma, Y.; Batzill, M. Molecular Beam Epitaxy of the Van Der Waals Heterostructure Mote2 on Mos2:

- Phase, Thermal, and Chemical Stability. 2D Mater. 2015, 2 (4), 044010.
- (26) Mirabelli, G.; McGeough, C.; Schmidt, M.; McCarthy, E. K.; Monaghan, S.; Povey, I. M.; McCarthy, M.; Gity, F.; Nagle, R.; Hughes, G.; Cafolla, A.; Hurley, P. K.; Duffy, R. Air Sensitivity of Mos2, Mose2, Mote2, Hfs2, and Hfse2. *J. Appl. Phys.* **2016**, *120* (12), 125102.
- (27) Martincová, J.; Otyepka, M.; Lazar, P. Is Single Layer Mos2 Stable in the Air? *Chem. Eur. J.* **2017**, 23 (53), 13233–13239.
- (28) Levita, G.; Restuccia, P.; Righi, M. C. Graphene and Mos2 Interacting with Water: A Comparison by Ab Initio Calculations. *Carbon* **2016**, *107*, 878–884.
- (29) Li, Q.; Zhou, Q.; Shi, L.; Chen, Q.; Wang, J. Recent Advances in Oxidation and Degradation Mechanisms of Ultrathin 2d Materials under Ambient Conditions and Their Passivation Strategies. *J. Mater. Chem. A* **2019**, 7 (9), 4291–4312.
- (30) Yalon, E.; Aslan, Ö. B.; Smithe, K. K. H.; McClellan, C. J.; Suryavanshi, S. V.; Xiong, F.; Sood, A.; Neumann, C. M.; Xu, X.; Goodson, K. E.; Heinz, T. F.; Pop, E. Temperature-Dependent Thermal Boundary Conductance of Monolayer Mos2 by Raman Thermometry. ACS Appl. Mater. Interfaces 2017, 9 (49), 43013—43020
- (31) Bäuerle, D. W. Laser Processing and Chemistry; Springer: Berlin, Heidelberg, 2011.
- (32) Heavens, O. S. Optical Properties of Thin Solid Films. Dover: New York1991.
- (33) Chakraborty, B.; Bera, A.; Muthu, D.; Bhowmick, S.; Waghmare, U. V.; Sood, A. Symmetry-Dependent Phonon Renormalization in Monolayer Mos 2 Transistor. *Phys. Rev. B: Condens. Matter Mater. Phys.* **2012**, 85 (16), 161403.
- (34) Lee, C.; Yan, H.; Brus, L. E.; Heinz, T. F.; Hone, J.; Ryu, S. Anomalous Lattice Vibrations of Single- and Few-Layer Mos2. *ACS Nano* **2010**, *4* (5), 2695–2700.
- (35) Mak, K. F.; Lee, C.; Hone, J.; Shan, J.; Heinz, T. F. Atomically Thin Mos 2: A New Direct-Gap Semiconductor. *Phys. Rev. Lett.* **2010**, 105 (13), 136805.
- (36) Tongay, S.; Zhou, J.; Ataca, C.; Liu, J.; Kang, J. S.; Matthews, T. S.; You, L.; Li, J.; Grossman, J. C.; Wu, J. Broad-Range Modulation of Light Emission in Two-Dimensional Semiconductors by Molecular Physisorption Gating. *Nano Lett.* **2013**, *13* (6), 2831–2836.
- (37) Saltiel, S. M.; Neshev, D. N.; Krolikowski, W.; Arie, A.; Bang, O.; Kivshar, Y. S. Multiorder Nonlinear Diffraction in Frequency Doubling Processes. *Opt. Lett.* **2009**, *34* (6), 848–850.
- (38) Berger, V. Nonlinear Photonic Crystals. Phys. Rev. Lett. 1998, 81 (19), 4136.
- (39) Mateos, L.; Molina, P.; Galisteo, J.; López, C.; Bausá, L. E.; Ramírez, M. O. Simultaneous Generation of Second to Fifth Harmonic Conical Beams in a Two Dimensional Nonlinear Photonic Crystal. *Opt. Express* **2012**, *20* (28), 29940–29948.
- (40) Jung, G.-H.; Yoo, S.; Park, Q.-H. Measuring the Optical Permittivity of Two-Dimensional Materials without a Priori Knowledge of Electronic Transitions. *Nanophotonics* **2019**, 8 (2), 263–270.
- (41) Reitz, J.; Milford, F.; Christy, R. Foundations of Electromagnetic Theory, 4th ed.; Addison-Wesley: Reading, MA, USA, 1993.